Australasian Physical & Engineering Sciences in Medicine (2019) 42:83–90
https://doi.org/10.1007/s13246-018-0714-z

SCIENTIFIC PAPER

Estimation of the minimum detectable phase change of surface coil for neural current MRI

Seyed Mehdi BagheriMofidi[1]

Received: 19 May 2018 / Accepted: 15 November 2018 / Published online: 22 November 2018

Abstract

Neuronal current magnetic resonance imaging (NC-MRI) is a new method in functional imaging of the brain that could cause the alteration in the phase of magnetic resonance signal. The phase variance is defined as the inverse of the signal to noise ratio (SNR). The intrinsic SNR of the MRI signal is characterized by the coil performance. We evaluated the relation between the geometry and the shape of coils in order to find the minimum detectable change in the signal phase and the possibility of direct detection of neuronal activity by MRI. Full wave equations were solved by the finite element method to calculate the SNR for circular, elliptical, and square shape surface coils. The simulation was repeated for Larmor frequencies of 64 MHz and 85.2 MHz and the coil sizes between 1.5 and 7.5 cm. Relative intrinsic signal to noise ratio (rISNR) of coils with a respect to a selected reference coil and a reference point in the sample was estimated. The circular coil had higher rISNR than other shapes. The increase of the strip width in the coils raised the rISNR 5–20%. For typical imaging parameters, rISNR reference was about 66 which led to a minimum detectable change in MRI signal phase of 0.87° (11.4 nT). It may also be reduced up to tenfold in a 1.5 cm circular coil. Detection of subtle phase signal change due to neuronal activity in surface coils needs a large amount of data acquisition and averaging, but it is intrinsically feasible.

Keywords Neuronal current MRI · Phase signal change · Surface coil · Geometry · SNR · Sample resistance

Introduction

Detection of magnetic resonance (MR) signal changes due to the electrical activity of neurons were proposed as a new method for the functional imaging of the brain [1–6]. The axial current which flows in the activated neurons produces a neuronal magnetic field (NMF) that alters the phase and the magnitude of MR signal [7, 8]. High signal to noise ratio (SNR) coils could detect such subtle phase signal change (PSC) due to neuronal activity if the imaging parameters are selected correctly [9, 10]. The generated image is called neuronal current MRI (NC-MRI).

Radiofrequency (RF) coils are used as the receiver of the MR signal [11, 12]. Different types of RF coils have been designed based on several factors such as SNR [13], homogeneity of response [14], and the anatomy of the imaging area [15, 16]. According to their shape, RF coils can be divided into volume coils and surface coils. Surface coils have high SNR near to the main plane; however, it drops fast with distance from the coil [17–19]. In addition, to increase the homogeneity of response in the field of view, an array of surface coils was developed [20].

SNR of coils increases by working frequency [18, 21, 22]. In addition, SNR and homogeneity of response depend on some geometric parameters of the coils and the sample [21–25]. Even the air gap between the coil and the sample changes the quality factor [22, 26]. It was shown that the type of conductor could change coil resistance and the quality factor of the coil [27].

In this work, we investigate the intrinsic SNR (ISNR) of circular, square, and elliptical shape surface coils for 1.5 T and 2 T MRI system. Development and tuning of such a large number of coils is tedious work, so the selected method for analyzing of SNR was based on finite element solving of full wave equations. The resistance of simulated coils was compared to the reported experimental data to validate the simulated results. Our final goal was to find which geometry and size of the single surface coil has potential to detect PSC.

✉ Seyed Mehdi BagheriMofidi
m.bagherimofidi@aliabadiau.ac.ir

[1] Department of Biomedical Engineering, Aliabad Katoul Branch, Islamic Azad University, Aliabad Katoul, Iran

Methods

Theory

It can be shown that variance of phase signal of MRI (σ_φ) is equal to the inverse of ISNR [28]:

$$\sigma_\varphi = \frac{1}{ISNR} \propto \frac{\sqrt{R_{tot}}}{{f_0}^2 B^*_{xy}} \tag{1}$$

In which, f_0 is resonance frequency or Larmor frequency, R_{tot} is total resistance including sample loading (R_{sample}), copper resistance (R_{copper}), and extra resistance like the radiative loss (R_{irr}), and B^*_{xy} is the complex conjugate of the receiver transverse magnetic field (x–y surface) at a desired point produced by a unit current flowing in the coil, and it is defined by [29]:

$$B^*_{xy} = B^- = \frac{B^*_x + iB^*_y}{2} = \left(\frac{B_x - iB_y}{2}\right)^* \tag{2}$$

It is worth noting that in the Eq. (1), the higher ISNR implies the lower variance of phase, so it means a smaller minimum detectable phase. The neuronal current generates the magnetic field around the activated neurons. It can alter the phase of MRI signal [8]. So, the minimum detectable phase signal implies the minimum detectable NC-MRI signal.

To evaluate Eq. (1), a full wave solution was applied to different coil geometries. For low fields, it is possible to use the magneto-static approximation, and the Biot–Savart law is applied [30, 31], but when the wavelength is comparable to the coil structure, full wave analysis is necessary. The full wave equation for the electrical field (E) in the frequency domain is formulated as:

$$\nabla \times \mu_r^{-1}(\nabla \times \mathrm{E}) - k_0^2\left(\varepsilon_r - \frac{j\sigma}{\omega_0 \varepsilon_0}\right)\mathrm{E} = 0 \tag{3}$$

In which, σ is conductivity, ε_r and ε_0 are relative and vacuum permittivity, $k_0 = \omega\sqrt{\varepsilon_0 \mu_0}$ is the wave number in the vacuum, and μ_r and μ_0 are relative and vacuum permeability, respectively. Angular resonance frequency (ω_0) is calculated from the external magnetic field (B_0) multiplication in the gyromagnetic ratio ($\omega = \gamma B_0$). Magnetic fields (B) could be evaluated as:

$$\nabla \times \mathrm{E} = -\mathrm{j}\omega\mathrm{B} \tag{4}$$

Sample load is calculated by:

$$\frac{1}{2}R_{sample}I^2 = \frac{1}{2}\sigma \int\limits_{sample} |\mathrm{E}|^2 dV \tag{5}$$

Also, total resistance (R_{tot}) of the coil is equal to the measured impedance in the input port which is the voltage divided by the current of the port.

Because of skin depth effect at high frequency, the current flows in the thin exterior layer of the conductor. The thickness of the layer in copper is ($\sigma \approx 58.5 \times 10^6 (\mathrm{S/m})$) [32]:

$$\delta = \sqrt{\frac{1}{\pi f_0 \sigma \mu_0}} \tag{6}$$

If the penetration depth is small compared to the radius of the cross-section for the wire coil or half of the thickness for the strip coil, the classical resistance of coil per unit length can be calculated as:

$$R_{copper\_clas} = 1/\sigma A \tag{7}$$

where A is the current cross-section. It is equal to $A = 2\pi a\delta$ for a wire coil with radius a and $A = 2w\delta$ for a strip coil with width w. Because the current tends to flow in the edge of the conductor, there is also a lateral skin effect for the conductor with rectangular cross section which introduces another type of resistance for the strip coils [32]. Experiments have shown that the lateral to classical skin effect resistance ratio is about 1.5 and 2.0 for 64.0 MHz and 85.2 MHz respectively [32]. Therefore, the copper resistance for the strip conductor is:

$$\begin{aligned} R_{strip\ copper} &\approx 2.5 \times R_{copper\_clas} @ 64\ \mathrm{MHz} \\ R_{strip\ copper} &\approx 3.0 \times R_{copper\_clas} @ 85.2\ \mathrm{MHz} \end{aligned} \tag{8}$$

Because the coils are constructed from the perfect electrical conductor (PEC) in our simulation, the estimated total impedance is the sum of the sample load and the radiative resistance. In addition, the copper resistance was calculated theoretically except for the wire coil (see "Simulation" section).

Coil and sample geometry

We simulated three different coil shapes: circular, elliptical, and square (Fig. 1). The size of a coil was considered as the radius for circular coils, the minor radius for elliptic coils, and the half side for square coils. The size varied from 1.5 to 7.5 cm with a 1.5 cm step. The major radius of the elliptical coils was 7.5 cm. The coils were formed as strip coils with a width of 2 mm and 8 mm. In addition, circular wire coils were simulated with mentioned radius. The cross-section diameter of the wire was 2 mm.

The sample load (phantom) is a rectangular cube with a size of $37 \times 25 \times 22$ cm^3 and dielectric parameters of $\varepsilon_r = 77.85$, $\sigma = 0.3865$ (S/m) [22, 33]. The distance of a coil to the sample face was 1.5 cm.

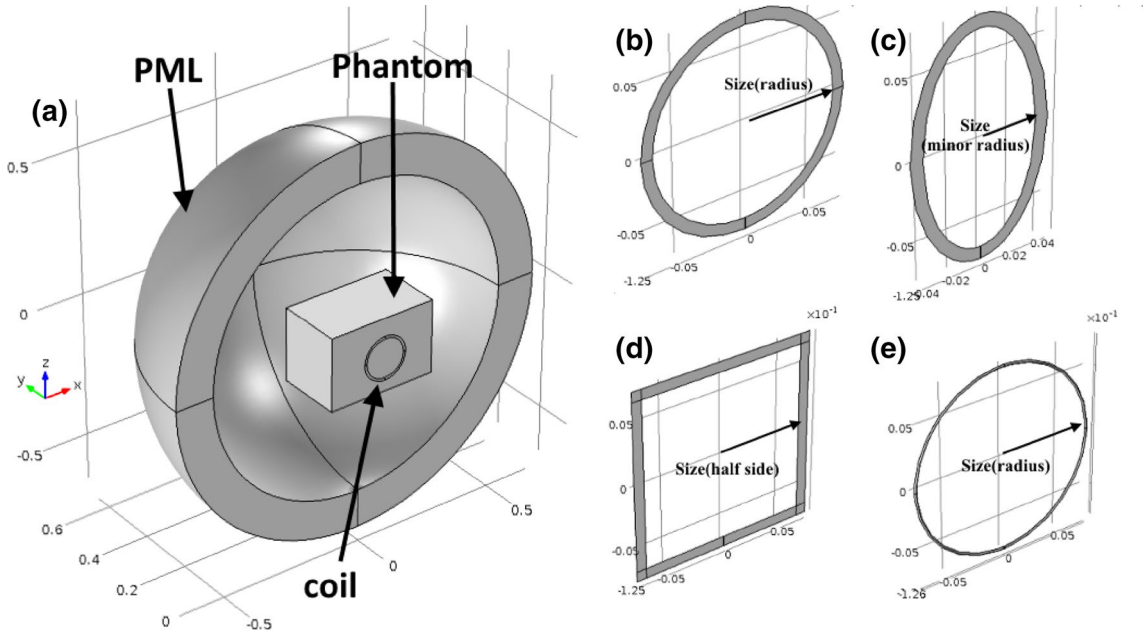

Fig. 1 **a** General geometry of coil simulation, half of the perfect match layer (PML) was hidden. Simulated coil geometries are **b** circular strip coil, **c** elliptical strip coil, **d** square strip coil, **e** circular wire coil. The concept of size for each shape is shown

Simulation

In order to solve Eq. (3), different algorithms could be used such as the method of moment (MoM), finite difference time domain (FDTD), and finite element method (FEM) [34]. Here, we used COMSOL Multiphysics software based on FEM and the results were compared with the FDTD algorithm. In addition, to validate our simulations approach, the total resistance of some simulated coils was compared with experimental data in the literature.

The geometry of the coils was defined in the software (Fig. 1). The periphery of the simulation environment was limited by the spherical perfect matched layer (PML). The coils were modeled as PEC except for the circular wire coil that was modeled as a copper shell with an impedance boundary condition to consider skin effects in the simulation. A lumped current port was considered to trigger the coil. The sum of the load and the radiative resistance was calculated from the total power delivered to the port. The simulations were repeated for 64 MHz and 85.2 MHz equal to the Larmor frequency of protons at 1.5 T and 2 T, respectively. In addition, to validate our simulation approach, the resistive parameters of a 7.5 cm circular wire coil were calculated by simulation when the phantom is not presented. The results were compared with the literature data [35].

To compare the SNR of the coils, a reference point on a coil was considered. The reference coil was the circular strip coil with a radius of 7.5 cm, 8 mm width and frequency 64 MHz, and the reference point was at the central line of the coil on the anterior surface of the sample. It was named $ISNR_{ref}$. Then the relative intrinsic SNR (rISNR) was defined for each coil as:

$$rISNR \triangleq \frac{ISNR}{ISNR_{ref}} = \frac{\omega_0^2 B_{xy}^*}{\omega_{0,\,ref}^2 B_{xy,\,ref}^*} \frac{\sqrt{R_{ref}}}{\sqrt{R_{tot}}} \tag{9}$$

Results

The size of coils and the resonance frequency affected the total resistance. The results are shown in Fig. 2. The circular coils have minimum total resistance at all sizes and the simulated frequencies. In addition, the strip coil with 2 mm width and the circular wire coils have the same resistance. Because the elliptical coil has the largest size among the coils, it has the highest resistance for sizes less than 6 cm. The total resistance of the square coil is dominant if the size of the coil is more than 6 cm.

The assessment of the contribution of the resistance type to the total resistance demonstrates that radiative loss is negligible, but the copper and the sample resistance have competing contributions to the total resistance, depending on the size and geometry of the coils (Fig. 3). When the size of the coils is less than 1.5 cm for the elliptical strip coil and the circular wire coil or less than 3 cm for the circular strip coil and the square strip coil, the copper resistance dominates, otherwise the sample resistance is main component. It must be noted that near these sizes, both types of resistance

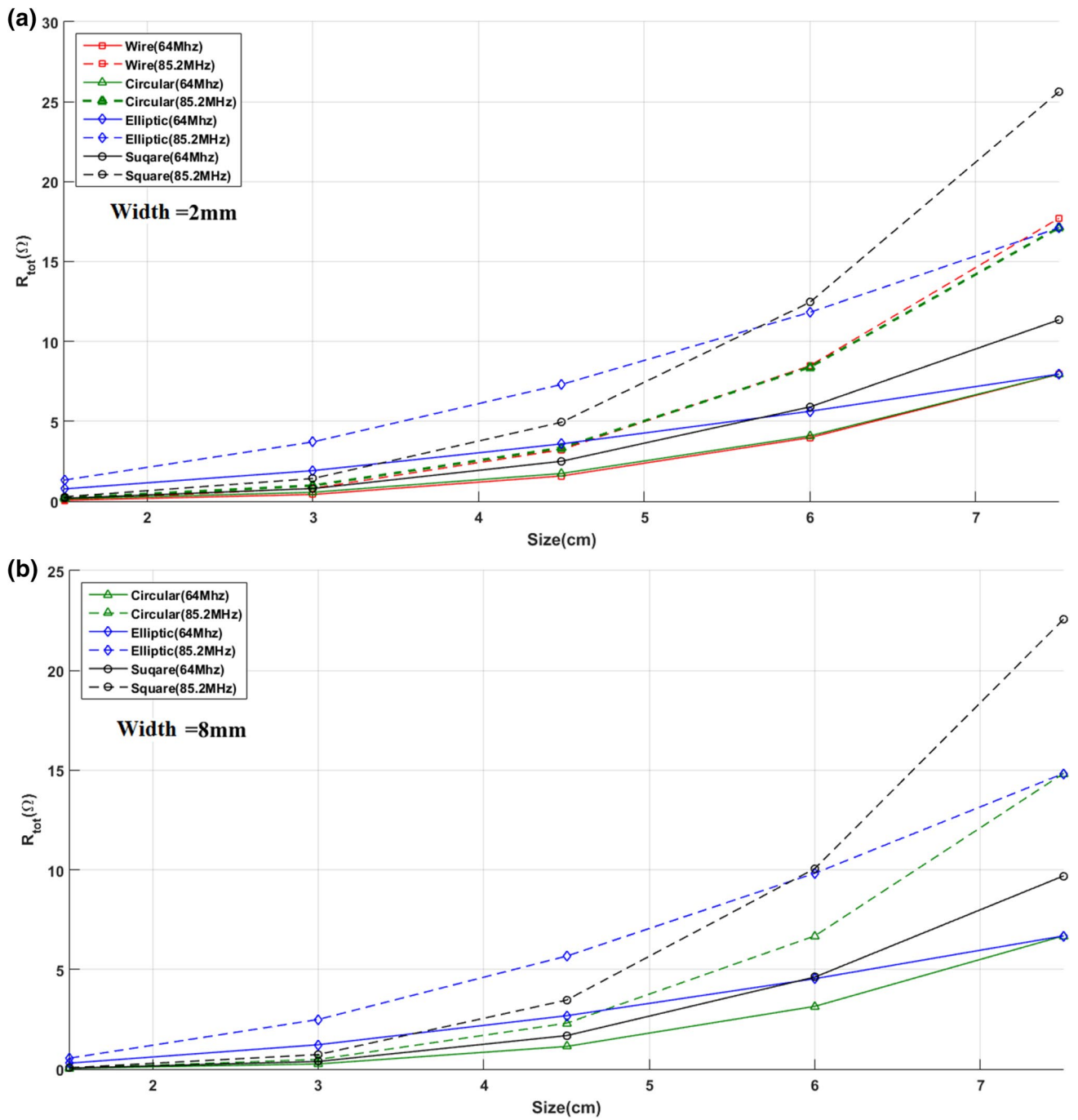

Fig. 2 The total resistance of different geometries of surface coils at 64 MHz (solid lines) and 85.2 MHz (dashed lines) for strip width or wire diameter **a** 2 mm and **b** 8 mm. Size is the radius, minor radius, and half side of the square for circular, elliptic and square coils, respectively

have comparable values and can not be ignored. Moreover, copper resistance contribution decreases to about 20% or less for sizes more than 4.5 cm. Because the dependency of sample load resistance to the frequency is more than the copper resistance [22], the contribution of sample load at 85.2 MHz is larger than 64 MHz. The results are also valid for the 8 mm width (not shown).

To validate our simulation with previous works, total resistance, copper resistance, and radiative resistance were evaluated for the 7.5 cm circular wire without the sample, at 63.9 MHz, 85.2 MHz, and 127.8 MHz (Table 1). These results were compared with the simulation of the same coil in the CST-SW Suite, HFSS and analytic results [35]. In CST-SW Suite and HFSS, the volume mesh was applied

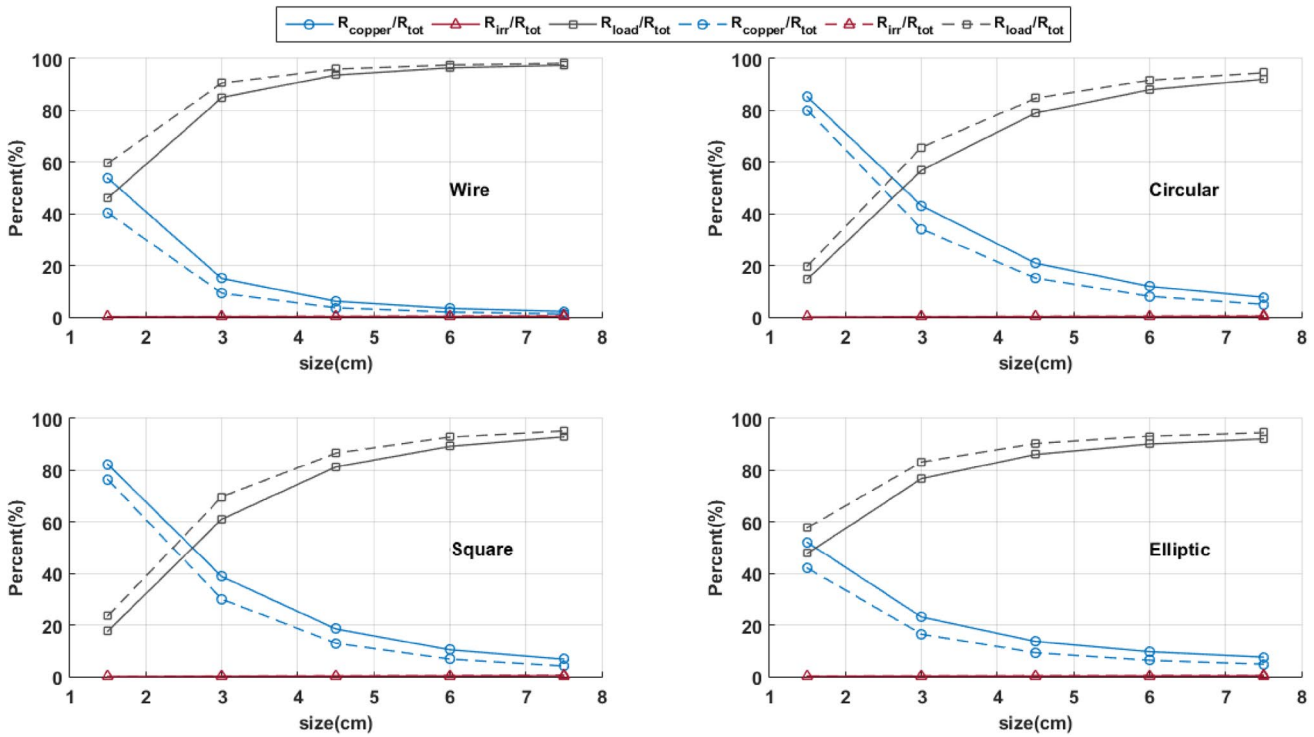

Fig. 3 The contribution of resistance components to the total resistance at 64 MHz (solid lines) and 85.2 MHz (dashed lines) for strip width or wire diameter 2 mm

Table 1 Comparison of total resistance, copper resistance, and radiative resistance between different simulation software and analytic calculation for the circular wire coil

	Frequency = 127.8 MHz			Frequency = 85.2 MHz			Frequency = 63.9 MHz		
R = 7.5 cm	R_{irr}	R_c	R_{tot}	R_{irr}	R_c	R_{tot}	R_{irr}	R_c	R_{tot}
COMSOL	571.38	333.08	904.48	81.62	211.68	293.31	22.85	169.42	192.27
CST-MW[a]	574.69	345.109	919.8	85.03	218.97	304	21.63	175.37	197
HFSS[a]	561.03	310.80	871.83	80.60	213.7	294.30	22.91	173.39	196.30

The resistances are in mΩ

[a]Ref. [35]

to the copper wire, while in our model the copper wire was considered as a shell with impedance boundary condition to estimate skin effect. The difference in the simulation method and the mesh size could be the main reasons for small difference between the results. Moreover, our method has resistance values close to the analytic results. The analytic expression was used for the calculation of the radiative resistance is only valid for very small coil size with respect to the wavelength which was resulted in the large difference between the simulation and the analytic values. In addition, Table 2 shows that there is good agreement between FEM calculations of sample load in this study with previous experimental results in the literature [22] for the same sample and coil size at 64 MHz. The table also contains the results from FDTD and vector potential calculation (VPC) methods.

Table 2 Comparison the sample load resistance between the experimental results and simulations for the circular wire coil

Frequency = 64 MHz	R = 1.5 cm	R = 6 cm
Measurement[a]	27 mΩ	3.8Ω
FEM (COMSOL)	27.005 mΩ	3.8369Ω
FDTD[a]	26 mΩ	4.1Ω
VPC[a]	22 mΩ	2.7Ω

[a]Ref. [22]

The rISNR distribution is illustrated in Fig. 4 for the circular strip coil with 2 mm width for transverse plane passes through the coil center. Dielectric properties of the sample could disturb the magnetic field of the coil which results in the inhomogeneity of response (Fig. 4). A similar distribution

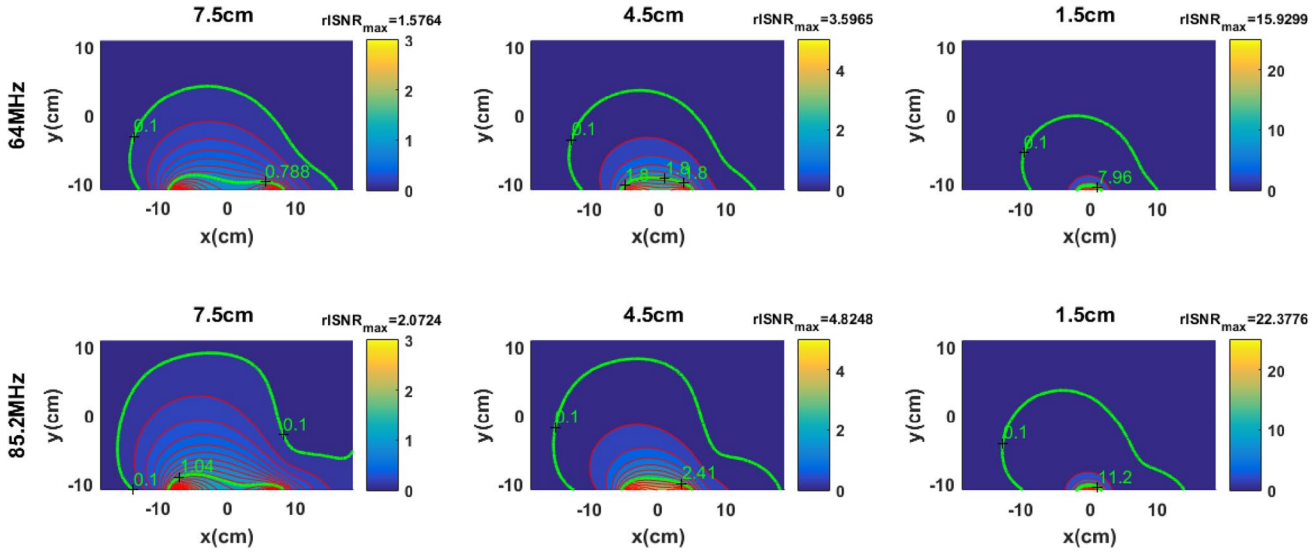

Fig. 4 Distribution of rISNR for circular strip coil with 2 mm width on the surface through center of coil (z = 0) for radius of 7.5 cm (left column), 4.5 cm (middle column) and 1.5 cm (right column) at 64 MHz (top row) and 85.2 MHz (bottom row). The contour level of 0.1 and half of maximum rISNR was shown for comparison of all coils (green). Each column has the same color map and contour level. In addition, maximum rISNR of the surface was noted at top of each color map

was achieved for the wire coil and other geometries except that maximum rISNR changed. The increase of the size of the coil reduces the homogeneity of response and maximum rISNR, but the depth which rISNR drops below 0.1, increases (tenth value depth in Fig. 4). The tenth value depth (TVD) at 85.2 MHz is also more than 64 MHz. Maximum rISNR for a size of 1.5 cm with respect to 7.5 cm could be up to ten-fold. In addition, it increases linearly with frequency in good agreement with analytical calculations [17]. The maximum of rISNR occurs under the strip or the wire for large coils, but for the small coil size, it reaches a maximum at the center of the coil.

In the sample, a volume was defined as the field of view to evaluate the homogeneity and average of rISNR. The upper face geometry was the same as the coil, and the depth is equal to the size of the coil (radius of circular, minor radius of elliptical, and the half side of the square). The average of the rISNR, standard deviation and maximum rISNR are reported in Table 3 for the FOV. One standard deviation from the mean of rISNR is about 50% in the FOV. It is in agreement with the common rule of thumb that the useful depth of the surface coil is about its radius. The smaller size coils have a minor improvement of homogeneity. While the increase of strip width increases rISNR from 5 to 20%, it somewhat raises the inhomogeneity.

Discussion

In this research, the effect of geometry, size, conductor type, and frequency of the surface coil on the relative intrinsic signal to noise was investigated. Finite element analysis was used to calculate the distribution of response of each coil.

We assumed that the dielectric properties of the sample are equal for both frequencies. Practically, the conductivity and permittivity values change with frequency. For example the grey matter conductivity and relative permittivity change about 6% and 12% respectively for 64 MHz and 85.2 MHz. We found that such variations have a small effect on the results.

The simulation demonstrates that SNR drop in the sample is fast for smaller coil size. On the other hand, these coils have better SNR near the coil plane that increases the probability of PSC signal detection. From a practical viewpoint, the most of neuronal activity happens on the gray matter which is about 3 cm under the skull, and the thickness of grey matter is approximately 2 mm [36], therefore, the small size coils as large as ~ 3 cm are the best size for detection of PSC.

To calculate copper resistance by FEM analysis, the mesh size in the volume of copper must be lower than the

Table 3 Average rISNR and its standards deviation as a percentage with respect to mean rISNR on the defined FOV in the sample

Frequency (MHz)	Width (diameter) (mm)	size (cm)	Circular wire	Circular strip	Square strip	Elliptic strip
64	2	1.5	7.24 ± 40.1% (17.7)	6.44 ± 42.7% (16.5)	3.95 ± 41.2% (10.04)	2.42 ± 35.5% (4.90)
		3	2.86 ± 47.3% (7.22)	2.84 ± 49.0% (7.34)	2.06 ± 46.4% (5.28)	1.46 ± 40.9% (3.30)
		4.5	1.35 ± 49.2% (3.61)	1.36 ± 50.4% (3.70)	1.06 ± 47.8% (2.88)	0.93 ± 44.7% (2.4)
		6.0	0.77 ± 50.1% (2.31)	0.78 ± 51.0% (2.43)	0.63 ± 48.6% (1.95)	0.65 ± 48.2% (1.95)
		7.5	0.50 ± 50.7% (1.66)	0.49 ± 51.5% (1.69)	0.42 ± 49.4% (1.41)	×
	8	1.5	×	4.74 ± 47.8% (14.8)	4.55 ± 48.5% (15.00)	3.04 ± 40.6% (7.21)
		3	×	3.00 ± 54.7% (9.13)	2.55 ± 53.0% (7.51)	1.68 ± 45.5% (4.11)
		4.5	×	1.43 ± 54.9% (4.21)	1.19 ± 52.5% (3.49)	1.02 ± 48.4% (2.83)
		6.0	×	0.81 ± 54.5% (2.63)	0.68 ± 52.3% (2.16)	0.70 ± 51.4% (2.18)
		7.5	×	0.52 ± 54.3% (1.80)	0.44 ± 52.4% (1.54)	×
85.2	2	1.5	10.4 ± 40.3% (25.1)	9.19 ± 41.8% (23.2)	5.8 ± 40.9% (14.63)	3.35 ± 35.3% (6.81)
		3	3.75 ± 46.8% (9.27)	3.27 ± 48.4% (8.42)	2.8 ± 49.5% (6.95)	1.92 ± 40.7% (4.38)
		4.5	1.74 ± 48.5% (4.82)	1.75 ± 49.8% (5.04)	1.39 ± 47.4% (3.86)	1.21 ± 44.5% (3.13)
		6.0	0.99 ± 49.6% (2.97)	1.00 ± 50.5% (3.11)	0.81 ± 48.5% (2.5)	0.85 ± 48.1% (2.55)
		7.5	0.65 ± 50.3% (2.26)	0.64 ± 51.1% (2.22)	0.54 ± 49.3% (1.86)	×
	8	1.5	×	6.90 ± 48.0% (23.1)	6.72 ± 47.5% (22.39)	4.06 ± 40.5% (9.64)
		3	×	3.96 ± 54.1% (12.0)	3.35 ± 52.5% (9.74)	2.16 ± 45.3% (5.32)
		4.5	×	1.85 ± 54.3% (5.43)	1.54 ± 52.1% (4.47)	1.31 ± 48.2% (3.64)
		6.0	×	1.04 ± 54.0% (3.38)	0.87 ± 52.1% (2.79)	0.90 ± 51.1% (2.75)
		7.5	×	0.67 ± 54.0% (2.32)	0.57 ± 52.3% (2.00)	×

Maximum rISNR is noted in the parentheses

skin effect size ($\delta = 8.2$ µm for 64 MHz, and $\delta = 7.1$ µm for 85.2 MHz). Because of limited computational performance, it was not possible to use such small size meshes, and the copper resistance was calculated analytically except for the wire coil that had good conformance with analytic values (Table 1). Moreover, the increase in the number of mesh elements (~ 35%) in the peripheral region of coil only changed the value of resistance by about 1%.

For typical MRI imaging parameters in the brain (TE = 5 ms, TR = 400 ms, T1 = 955 ms, T2 = 65 ms, flip angle = 30°, FOV = 22cm × 22 cm, slice thickness = 6 mm, 256 × 256, BW = 93,632 Hz), $ISNR_{ref}$ was calculated the about 66 [37]. It is equal to the phase noise level of 0.87°, or a minimum detectable magnetic field of 11.4 nT for a single acquisition of a phase image. On the other hand, the previous simulation for stimulation of cortical column network showed that PSC could be between 100 and 500 µrad [7, 8]. In order to detect such slight signals, it must be averaged to reduce the noise level. Averaging raises SNR by the square root of the number of acquisitions. For example, in this case, 918 to 22,957 times of data acquisition is needed from ideal condition. The decrease of coil size could increase the ISNR, so acquisition time could be reduced. For example, at 85.5 MHz for 3.0 cm circular strip coil with 8 mm width, mean rISNR in the FOV could be about 4 ($SNR = 4 \times ISNR_{ref}$), and data averaging reduces to 58 up to 1435 readings. It is noteworthy that physiological noise could increase the total noise, so the SNR in the alive sample is less than previous estimation [38]. It must also be noted that blood oxygenation level-dependent (BOLD) signal could contaminate the signal change due to neuronal activity, so differentiating between them is hard [39].

Conclusion

Our simulation with different geometries shows that the circular coil have higher SNR than other geometries. The minimum detectable PSC for a circular strip coil with radius of 7.5 cm is about 15 mrad. It decreases up to fourfold for a 3 cm coil size. However, the direct detection of PSC signal due to neuronal activity which is about 100 µrad, needs the large repetitions of MRI acquisition to increase SNR, but it is intrinsically possible.

Acknowledgements This work was supported by Aliabad Katoul Branch, Islamic Azad University.

Compliance with ethical standards

Conflict of interest Seyed Mehdi BagheriMofidi declares that he has no conflict of interest.

Ethical approval This article does not contain any studies with human participants or animals performed by any of the authors.

References

1. Bodurka J, Bandettini PA (2002) Toward direct mapping of neuronal activity: MRI detection of ultraweak, transient magnetic field changes. Magn Reson Med 47(6):1052–1058
2. Xiong J, Fox PT, Gao JH (2003) Directly mapping magnetic field effects of neuronal activity by magnetic resonance imaging. Hum Brain Mapp 20(1):41–49. https://doi.org/10.1002/hbm.10124
3. Luo Q, Jiang X, Gao JH (2011) Detection of neuronal current MRI in human without BOLD contamination. Magn Reson Med 66(2):492–497. https://doi.org/10.1002/mrm.22842
4. Poplawsky AJ, Dingledine R, Hu XP (2012) Direct detection of a single evoked action potential with MRS in Lumbricus terrestris. NMR Biomed 25(1):123–130. https://doi.org/10.1002/nbm.1724
5. Huang J (2014) Detecting neuronal currents with MRI: a human study. Magn Reson Med 71(2):756–762
6. Sundaram P, Nummenmaa A, Wells W, Orbach D, Orringer D, Mulkern R, Okada Y (2016) Direct neural current imaging in an intact cerebellum with magnetic resonance imaging. Neuroimage 132:477–490
7. Du J, Vegh V, Reutens DC (2014) MRI signal phase oscillates with neuronal activity in cerebral cortex: implications for neuronal current imaging. Neuroimage 94:1–11. https://doi.org/10.1016/j.neuroimage.2014.03.015
8. BagheriMofidi SM, Pouladian M, Jameie SB, Tehrani-Fard AA (2016) Estimation of phase signal change in neuronal current MRI for evoke response of tactile detection with realistic somatosensory laminar network model. Australas Phys Eng Sci Med 39(3):717–726
9. Luo Q, Jiang X, Chen B, Zhu Y, Gao JH (2011) Modeling neuronal current MRI signal with human neuron. Magn Reson Med 65(6):1680–1689. https://doi.org/10.1002/mrm.22764
10. Kim D, Someya T, Sekino M (2013) Sensitivity of MRI for directly detecting neuronal electrical activities in rat brain slices. Conf Proc IEEE Eng Med Biol Soc 2013:1370–1373. https://doi.org/10.1109/EMBC.2013.6609764
11. Hoult D (2000) The principle of reciprocity in signal strength calculations—a mathematical guide. Concepts Magn Reson A 12(4):173–187
12. Hoult DI (2011) The principle of reciprocity. J Magn Reson 213(2):344–346. https://doi.org/10.1016/j.jmr.2011.08.005
13. Constantinides C, Angeli S, Gkagkarellis S, Cofer G (2011) Intercomparison of performance of RF coil geometries for high field mouse cardiac MRI. Concepts Magn Reson A 38(5):236–252
14. Ibrahim TS, Mitchell C, Schmalbrock P, Lee R, Chakeres DW (2005) Electromagnetic perspective on the operation of RF coils at 1.5–11.7 T. Magn Reson Med 54(3):683–690
15. Welker KM, Tsuruda JS, Hadley JR, Hayes CE (2001) Radio-frequency coil selection for MR imaging of the brain and skull base. Radiology 221(1):11–25
16. Vossen M, Teeuwisse W, Reijnierse M, Collins C, Smith N, Webb A (2011) A radiofrequency coil configuration for imaging the human vertebral column at 7 T. J Magn Reson 208(2):291–297
17. Hayes CE, Axel L (1985) Noise performance of surface coils for magnetic resonance imaging at 1.5 T. Med Phys 12(5):604–607
18. Schnell W, Renz W, Vester M, Ermert H (2000) Ultimate signal-to-noise-ratio of surface and body antennas for magnetic resonance imaging. IEEE Trans Antennas Propag 48(3):418–428
19. Kumar A, Bottomley PA (2008) Optimized quadrature surface coil designs. Magn Reson Mater Phys Biol Med 21(1):41–52
20. Roemer PB, Edelstein WA, Hayes CE, Souza SP, Mueller O (1990) The NMR phased array. Magn Reson Med 16(2):192–225
21. Kumar A, Edelstein WA, Bottomley PA (2009) Noise figure limits for circular loop MR coils. Magn Reson Med 61(5):1201–1209
22. Giovannetti G, Hartwig V, Landini L, Santarelli M (2011) Sample-induced resistance estimation in magnetic resonance experiments: simulation and comparison of two methods. Appl Magn Reson 40(3):351–361
23. Rojas R, Rodriguez AO (2007) Numerical study of the optimal geometry of MRI surface coils. In: Engineering in medicine and biology society, 2007. EMBS 2007. 29th Annual international conference of the IEEE, pp 3890–3893
24. Hassan A, Elabyed I, Mallow J, Herrmann T, Bernarding J, Omar A (2010) Optimal geometry and capacitors distribution of 7T MRI surface coils. In: Microwave conference (EuMC), 2010 European, IEEE, pp 1437–1440
25. Giovannetti G, Tiberi G, Tosetti M (2016) Finite element method-based approach for radiofrequency magnetic resonance coil losses estimation. Magn Reson 46(4):186–190
26. Doty FD, Entzminger G, Kulkarni J, Pamarthy K, Staab JP (2007) Radio frequency coil technology for small-animal MRI. NMR Biomed 20(3):304–325
27. Giovannetti G, Hartwig V, Landini L, Santarelli M (2010) Low-field MR coils: comparison between strip and wire conductors. Appl Magn Reson 39(4):391–399
28. Scott G, Joy M, Armstrong R, Henkelman R (1992) Sensitivity of magnetic-resonance current-density imaging. J Magn Reson 97(2):235–254
29. Vaidya MV, Collins CM, Sodickson DK, Brown R, Wiggins GC, Lattanzi R (2016) Dependence of B1+ and B1− field patterns of surface coils on the electrical properties of the sample and the MR operating frequency. Concepts Magn Reson B 46(1):25–40. https://doi.org/10.1002/cmr.b.21319
30. Giovannetti G, Landini L, Santarelli MF, Positano V (2002) A fast and accurate simulator for the design of birdcage coils in MRI. Magn Reson Mater Phys Biol Med 15(1):36–44
31. Giovannetti G (2016) Comparison between circular and square loops for low-frequency magnetic resonance applications: theoretical performance estimation. Magn Reson 46(3):146–155
32. Giovannetti G, Hartwig V, Landini L, Santarelli MF (2012) Classical and lateral skin effect contributions estimation in strip MR coils. Magn Reson 41(2):57–61
33. Taylor HC, Burl M, Hand JW (1997) Experimental verification of numerically predicted electric field distributions produced by a radiofrequency coil. Phys Med Biol 42(7):1395
34. Chen J, Feng Z, Jin J-M (1998) Numerical simulation of SAR and B/sub 1/-field inhomogeneity of shielded RF coils loaded with the human head. IEEE Trans Biomed Eng 45(5):650–659
35. Giovannetti G, Fontana N, Monorchio A, Tosetti M, Tiberi G (2017) Estimation of losses in strip and circular wire conductors of radiofrequency planar surface coil by using the finite element method. Magn Reson 47(3):e21358
36. Defelipe J (2011) The evolution of the brain, the human nature of cortical circuits, and intellectual creativity. Front Neuroanat. https://doi.org/10.3389/fnana.2011.00029
37. Hatada T, Sekino M, Ueno S (2005) Finite element method-based calculation of the theoretical limit of sensitivity for detecting weak magnetic fields in the human brain using magnetic-resonance imaging. J Appl Phys 97(10):10E109
38. Triantafyllou C, Hoge RD, Krueger G, Wiggins CJ, Potthast A, Wiggins GC, Wald LL (2005) Comparison of physiological noise at 1.5 T, 3 T and 7 T and optimization of fMRI acquisition parameters. Neuroimage 26(1):243–250. https://doi.org/10.1016/j.neuroimage.2005.01.007
39. Jiang X, Lu H, Shigeno S, Tan LH, Yang Y, Ragsdale CW, Gao JH (2014) Octopus visual system: a functional MRI model for detecting neuronal electric currents without a blood-oxygen-level-dependent confound. Magn Reson Med 72(5):1311–1319. https://doi.org/10.1002/mrm.25051